Editors' Suggestion   Featured in Physics

Chirality-Induced Spin Polarization over Macroscopic Distances in Chiral Disilicide Crystals

Kohei Shiota,[1] Akito Inui,[1] Yuta Hosaka,[1] Ryoga Amano,[1] Yoshichika Ōnuki,[2,3] Masato Hedo,[2] Takao Nakama,[2]
Daichi Hirobe [4] Jun-ichiro Ohe [5] Jun-ichiro Kishine,[4,6] Hiroshi M. Yamamoto [4]
Hiroaki Shishido [1] and Yoshihiko Togawa [1,*]

[1]*Department of Physics and Electronics, Osaka Prefecture University, 1-1 Gakuencho, Sakai, Osaka 599-8531, Japan*
[2]*Faculty of Science, University of the Ryukyus, Nishihara, Okinawa 903-0213, Japan*
[3]*RIKEN Center for Emergent Matter Science, Wako, Saitama 351-0198, Japan*
[4]*Research Center of Integrative Molecular Systems, Institute for Molecular Science, Okazaki, Aichi 444-8585, Japan*
[5]*Department of Physics, Toho University, Chiba 274-8510, Japan*
[6]*Division of Natural and Environmental Sciences, The Open University of Japan, Chiba 261-8586, Japan*

A spin-polarized state is examined under charge current at room temperature without magnetic fields in chiral disilicide crystals $NbSi_2$ and $TaSi_2$. We found that a long-range spin transport occurs over ten micrometers in these inorganic crystals. A distribution of crystalline grains of different handedness is obtained via location-sensitive electrical transport measurements. The sum rule holds in the conversion coefficient in the current-voltage characteristics. A diamagnetic nature of the crystals supports that the spin polarization is not due to localized electron spins but due to itinerant electron spins. A large difference in the strength of antisymmetric spin-orbit interaction associated with $4d$ electrons in Nb and $5d$ ones in Ta is oppositely correlated with that of the spin polarization. A robust protection of the spin polarization occurs over long distances in chiral crystals.

The concept of chirality is widely found in various phenomena in nature at all length scales and governs the symmetry properties of the system. The original meaning of chirality is characterized by a geometrical relationship of handedness [1]: a pair of objects that correspond to their mirrored images but are distinguishable from each other. They cannot be superimposed on their counterparts and do contain only the symmetry operation of pure rotation. In addition, the dynamical aspects of chirality [2,3], which could be referred to as dynamical chirality, has increased its importance, inspired by a variety of chirality-induced responses discovered in many research fields such as biochemistry [4], nano-optics [5], phonon [6], and magnetism [7]. An interplay between structural and dynamical chirality should play a key role in the mechanism underlying chirality-induced phenomena [8].

In this respect, chirality-induced spin selectivity (CISS) has attracted much attention. The CISS phenomena, where electrons flowing through a chiral material become spin polarized, have been demonstrated in chiral molecules via spin-polarized photocurrent emission [9] and tunneling transport experiments [10,11]. Quantitative understanding of the CISS remains an important issue [12].

Quite recently, it is found that a chiral inorganic crystal $CrNb_3S_6$ exhibits a spin-polarized state when the charge current is injected into the crystal [13]. A spin-polarized transport occurs in a linear regime of the current-voltage characteristics. Importantly, a robust protection of the spin polarization enables a nonlocal spin transport over one micrometer. This study leads to interesting arguments on a role of conduction electrons and localized electrons in the CISS response, which has been hardly considered in previous studies using chiral molecules. For instance, self-amplification of the spin polarization via the spin transfer torque within the crystal is discussed in order to cope with a huge population of spin-polarized electrons generated by the charge current [14]. Those are intriguing characteristics of the CISS in the chiral dichalcogenide crystal, which may provide a crucial clue in clarifying the CISS mechanism.

In this study, we focus on a different type of chiral crystals: chiral disilicide crystals $NbSi_2$ and $TaSi_2$ with the hexagonal structure. Importantly, the electronic band structures of $NbSi_2$ and $TaSi_2$ have already been studied experimentally and theoretically [15]. The ellipsoidal Fermi surface is split into two spin states because of an antisymmetric spin-orbit interaction (SOI) due to the chiral structure of crystals. This works as a splitting energy of the spin-dependent Fermi surfaces and its magnitude changes from 200 to 500 K in accordance with the existence of $4d$ conduction electrons in Nb and $5d$ ones in Ta [15]. Moreover, these crystals exhibit diamagnetism and thus no presence of the localized electron spins [16]. The itinerant nature of electrons contrasts with the situation of $CrNb_3S_6$.

In this respect, detecting the CISS response in such $NbSi_2$ and $TaSi_2$ crystals is worth examining in order to clarify the electronic nature of the CISS.

Here we investigate the spin-polarized state induced by the charge current application in $NbSi_2$ and $TaSi_2$ crystals. Indeed, the CISS response appears in these disilicide crystals. The location-sensitive CISS measurements including a nonlocal detection revealed a spin polarized transport over 10 μm, which also manifested in the experimental finding of the sum rule of the convert coefficient of the CISS signals. The origin of such a long-range spin polarized transport over the crystal would be a key element in modeling the CISS.

Bulk crystals of $NbSi_2$ and $TaSi_2$ were grown in an arch melting furnace via the Czochralski pulling technique. X-ray structure analysis of the obtained crystals including the Flack parameter evaluation indicates that the former and the latter crystals belong to the chiral space group of $P6_222$ and $P6_422$, respectively. The size of the unit cell is 0.4798 and 0.4784 nm along the a axis and 0.6592 and 0.6568 nm along the c axis in $NbSi_2$ and $TaSi_2$, respectively. The determination of crystalline chirality using x-ray diffraction was performed with a piece of the bulk crystal of about 100 μm in size and thus provides average information on the chirality because of the limitations in a spot size and brightness of the x-ray beam available at the laboratory. As described below, the electrical CISS measurements reveal that the crystals used in this study contain crystalline grains with the opposite handedness at a micrometer scale.

The spin-polarized state of the chiral crystal is detectable in the device shown in Fig. 1(b). First, the crystal becomes

FIG. 1. (a) Crystalline structures of a disilicide compound MSi_2 (M: transition metal) that belongs to the chiral space group of $P6_222$ or $P6_422$. (b) A secondary ion microscopy image of the $NbSi_2$ crystal with the tungsten (W) electrode fabricated for the CISS measurements. (c) Variations of the CISS measurements for chirality determination. The CISS voltage signal is detected in the transverse direction of the tungsten electrode located at the center when a charge current is applied along the c axis of the hexagonal structure in a part of the crystal.

spin polarized along the c axis when a charge current is injected into the crystal. The spin current diffuses into the detection electrode due to a gradient of chemical potential of spin-polarized electrons. Then, the spin diffusion current is converted into a charge current via an inverse spin Hall effect and finally detected as a voltage output along the detection electrode. Since the direction of spin polarization depends on the chirality of the crystal under study, it can be inferred from the sign of the slope of current-voltage characteristics. Details of the device operations are available in the literature [13].

The fabricated device is made of a micrometer-sized lamella of $NbSi_2$ or $TaSi_2$ crystal, which is picked up from the corresponding bulk crystal by using a focused ion beam machine. For example, the device in Fig. 1(b) uses the $NbSi_2$ lamella with a dimension of 50 μm in length (along the c axis), 11 μm in width, and 1 μm in thickness. The CISS detection electrode of tungsten (W) in 6 nm thickness is located at the center of the device, while the gold electrodes are beside it for the charge current injection.

In this device, the CISS voltage signal appears in the transverse direction of the tungsten electrode when the charge current is applied in a part of the crystal, as presented in Fig. 1(c). Note that the CISS signal can emerge even in a nonlocal configuration [13], in which the charge current is applied in an area separate from the location for the signal detection. Thus, the CISS measurements can be performed in several configurations of the current injection and the chirality is determined at various locations of the crystal. The present device works well for the location-sensitive CISS measurements.

To characterize the quality of the crystals used in the devices, an electrical resistivity was examined as a function of temperature. The electrical resistivity of the $NbSi_2$ crystal takes a value of 35 $\mu\Omega$ cm at 300 K with residual resistivity ratio of 160, while the $TaSi_2$ crystal exhibits 38 $\mu\Omega$ cm at the same temperature with residual resistivity ratio of 55. These values are consistent with the reported ones [15] and guarantee the quality of the crystals. The resistivity of tungsten was evaluated to be 284 $\mu\Omega$ cm in a separate experiment.

Figure 2 shows a dataset of the current-voltage characteristics obtained by the location-sensitive CISS measurements. All the CISS data are taken at room temperature and at zero magnetic field. When the charge current flows throughout the sample, the CISS signals appear and exhibit the negative and positive slope in the present $NbSi_2$ and $TaSi_2$ crystals, respectively, as shown in Fig. 2(a). This behavior indicates that both crystals have the opposite chirality, which agrees with the x-ray results. However, more importantly, the presence of the crystalline grains of different chirality within the crystals is revealed by the spatially resolved electrical CISS detection, as described below.

The CISS transport in the nonlocal configuration is shown in Figs. 2(b) and 2(c). Note that the location for
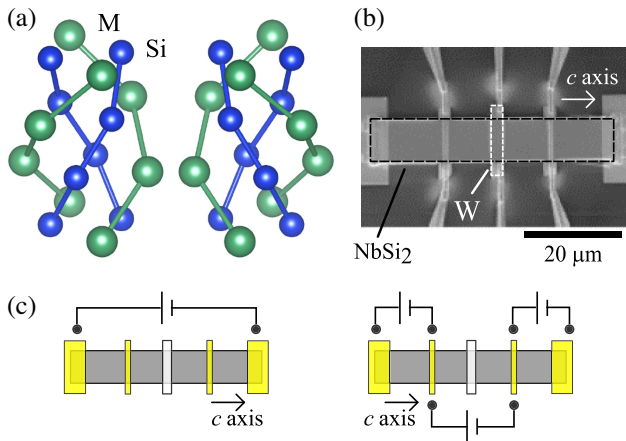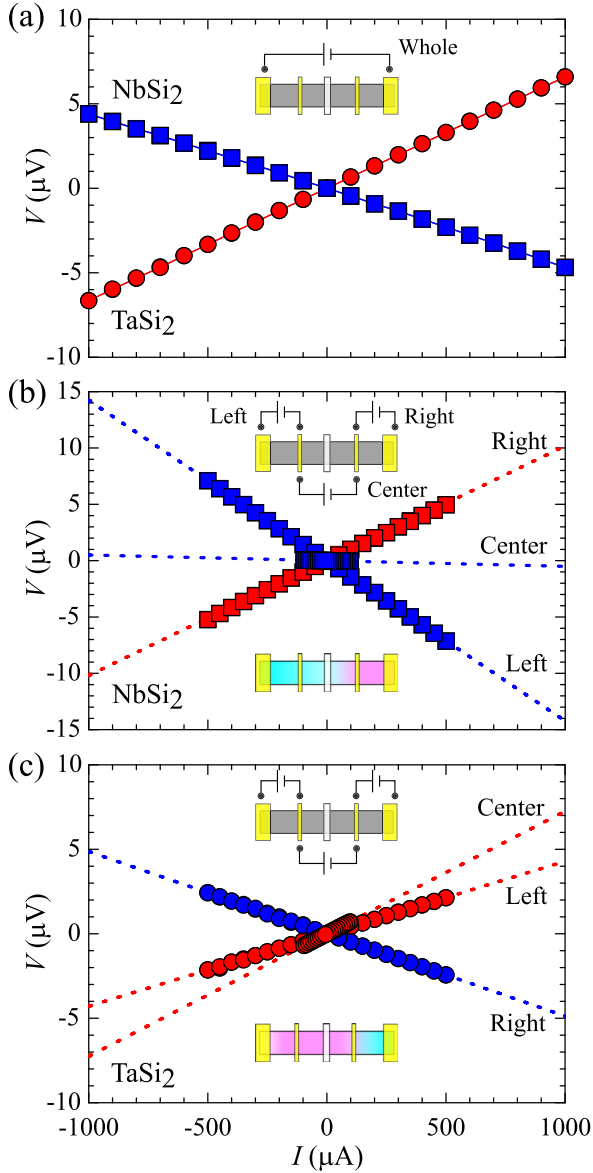
FIG. 2. A dataset of the CISS measurements for the $NbSi_2$ and $TaSi_2$ crystals with the tungsten electrode. Current-voltage characteristics are taken at room temperature at 0 T in the configuration of the current injection as schematically drawn in the insets. (a) The CISS signals of the $NbSi_2$ (square) and $TaSi_2$ (circle) crystals with the charge current applied throughout the samples. (b), (c) Location variations of the CISS signals when the charge current is applied in a part of the $NbSi_2$ and $TaSi_2$ crystals. The values of the slope are summarized in Table I. The insets show a schematic distribution of chirality grains in the lamellae, in which the handedness are distinguished by color.

TABLE I. A list of the slope values of the CISS signals for the $NbSi_2$ and $TaSi_2$ crystals with the tungsten electrode. The original data are available in Fig. 2.

Crystal	V/I (mΩ)				
	Whole	Left	Center	Right	Sum
$NbSi_2$	−4.52	−14.23	−0.50	10.18	−4.55
$TaSi_2$	6.62	4.29	7.25	−4.87	6.67

shown in Fig. 2(b). The present data indicate that the crystalline grains with different handedness exist in the crystal. Similar behavior is found in the $TaSi_2$ crystal, as shown in Fig. 2(c).

Another interesting feature of the CISS data is found in the different configuration of the current injection, labeled "center" in Figs. 2(b) and 2(c). In this case, the distance between two electrodes for the current injection is reduced in comparison with that used in the "whole" measurement in Fig. 2(a) with keeping the tungsten electrode in between. The intensity of the signal decreases approximately one tenth in the case of the $NbSi_2$ crystal, while the signal increases slightly in the $TaSi_2$ crystal. These data also support the existence of chirality grains in the crystals.

As a summary of the location-sensitive CISS measurements, the values of the slope V/I in each crystal are listed in Table I. A majority area exhibits the negative sign of V/I in the $NbSi_2$ crystal, while the positive in the $TaSi_2$ crystal. Based on these figures, a distribution of chirality grains can be speculated as schematically drawn in Fig. 2. This is likely to correspond to the chiral space group macroscopically determined by the x-ray structure analysis. Furthermore, the present electrical CISS measurements successfully identify the existence of the crystalline grains with the opposite chirality at a micrometer scale.

To interpret the meaning of the location-sensitive measurements, it is worth considering the summation of V/I taken for the three configurations of the current injection shown in Figs. 2(b) and 2(c). Their sum almost equals to the value for the current injection through the whole area given in Fig. 2(a). Namely, the sum rule holds in V/I. This means that the misalignment of the detection electrode hardly contributes to the transverse voltage. The total CISS signal over the crystal can be decomposed into a set of the signals originated from the divided area where the charge current is supposed to be applied individually. Moreover, V/I plays an important role as a conversion coefficient of the CISS response.

The present experimental finding indicates that the spin polarization generated by the charge current spreads out in the crystal with little attenuation so as to satisfy the sum rule. In fact, the spin polarization retains at least over 10 μm in the nonlocal CISS transport. If it decays rapidly in a length scale characterized by a spin diffusion length, which is typically less than 100 nm in the materials with a
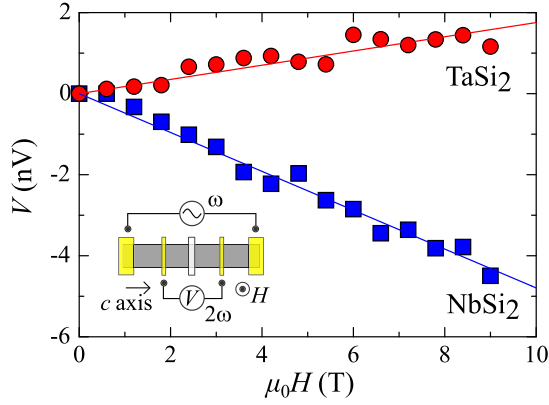
the current injection is 10 μm away from the detection electrode in these experiments. It is found that the sign of the slope changes, depending on the location where the charge current is applied. In the case of the $NbSi_2$ lamella, the CISS signals show the opposite sign of the slope against the current injection into the "left" and "right" sides, as

FIG. 3. The EMC signals taken at 200 K with the magnetic field applied in the direction perpendicular to the c axis of the NbSi$_2$ and TaSi$_2$ crystals. The sign of the slope indicates that of the EMC coefficient in the area for the voltage detection.

FIG. 4. The inverse CISS signals at room temperature at 0 T for the NbSi$_2$ (square) and TaSi$_2$ (circle) crystals with tungsten electrodes.

strong SOI, there is no room for holding the sum rule. Such a robust response of the CISS requires a nontrivial mechanism, which remains to be clarified.

To validate the results of the CISS response observed in the NbSi$_2$ and TaSi$_2$ crystals, the electrical magneto-chiral (EMC) transport [17] was examined in the center area of the same devices, as shown in Fig. 3. The EMC measurement is a complementary method for identifying the chirality of crystals since the sign of the EMC coefficient reflects the crystalline chirality, as demonstrated in CrNb$_3$S$_6$ [13,18].

The sign of the slope of the EMC signals is the opposite in the NbSi$_2$ and TaSi$_2$ crystals. This feature is consistent with that of the CISS signals observed in the same region in both crystals presented in Figs. 2(b) and 2(c). Thus, the chiral nature of the spin polarization is confirmed by the correlation between the EMC and CISS signals in the disilicide crystals. The largest EMC signal appears when the magnetic field is applied in the direction perpendicular to the c axis in the NbSi$_2$ and TaSi$_2$ crystals. Such behavior was also reported in chiral tellurium crystals [19].

A protection of the spin polarization over a long distance is favorable to confirming the reciprocal relationship of the CISS phenomena. In the inverse CISS process, the spin polarization induces the charge flow in the chiral crystal [13]. In the present device, when applying the charge current into the detection electrode, the spin polarization is initially induced beneath the electrode by the spin current injection via the spin Hall effect. Such a spin polarization would spread through the chiral crystal if it retains without attenuation. Consequently, the voltage would be generated across the crystal.

Figure 4 shows the inverse CISS signals at room temperature at 0 T. Linear current-voltage characteristics are observed in both crystals as seen in the direct CISS detection. The values of the slope are -4.60 mΩ for NbSi$_2$ and 6.70 mΩ for TaSi$_2$, respectively. These values are
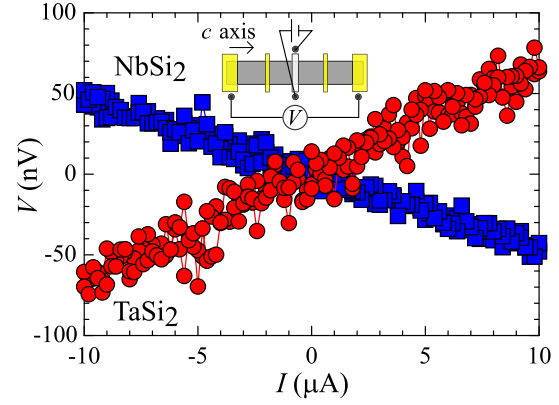
consistent with those for the direct CISS signals shown in Table I.

All the experimental results support that the CISS phenomena occur very robustly with a protection of the spin polarization over ten micrometers in the NbSi$_2$ and TaSi$_2$ crystals. Importantly, the disilicide crystals that contain only the itinerant electrons show the CISS response. Namely, the presence of localized electrons is not necessary to induce the CISS.

Splitting the Fermi surface was directly observed in NbSi$_2$ and TaSi$_2$ crystals by de Haas–van Alphen experiments [15]. The spin-dependent Fermi surfaces are schematically shown in Fig. 5. The structure of the ellipsoidal Fermi surface is the same in both crystals, while the splitting width of the Fermi surfaces changes systematically in accordance with the existence of 4d electrons in Nb and 5d ones in Ta. It is reported that the strength of the antisymmetric SOI is 209 K for the electron band in NbSi$_2$, while 493 K in TaSi$_2$ [15]. The maximum values of the CISS intensity shown in Table I are inversely correlated with those of the antisymmetric SOI. We may consider that the spin polarization phenomena would be much enhanced in the material with strong SOI. However, our results are likely to contradict with such a naïve idea but to be consistent with the experimental fact that the CISS effect is successfully observed in many kinds of chiral molecules that have tiny SOI [12].
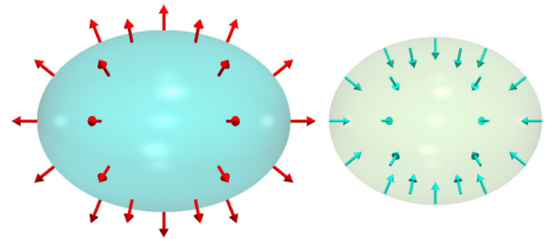

FIG. 5. A schematic drawing of the Fermi surface of a disilicide crystal.

In the disilicide compounds, the antisymmetric SOI is expressed by the form of $\alpha_1(k_x\sigma_x + k_y\sigma_y) + \alpha_2 k_z\sigma_z$ because of monoaxial crystal symmetry of the hexagonal $P6_222$ and $P6_422$ space group. The existence of the in-plane component in the wave number space allows a flipping process from the out-of-plane component to the in-plane ones and vice versa. However, once the spins flipped, the direction of spins should be instantaneously reoriented along the c axis under the charge current so as to protect the spin polarization robustly. Moreover, such a spin flip process should be compatible with a spin-polarized transport over long distances as well since the sum rule holds in the spin transport phenomena. A characteristic length of the long-range spin transport is at least beyond ten micrometers, which is much longer than the spin diffusion length and a mean free path of the conduction electrons. The mean free path is calculated to be about 30 nm at room temperature in $NbSi_2$ and $TaSi_2$ crystals from the experimental data [20]. A large difference in the length scale also indicates the importance of the long-range spin transport, which is clearly seen in the nonlocal experiments in the present study. Further theoretical considerations will clarify the mystery of the robust CISS response over macroscopic distances found in different categories of chiral materials [13].

---

[*] y-togawa@pe.osakafu-u.ac.jp

[1] L. Kelvin, in *Baltimore Lectures on Molecular Dynamics and the Wave Theory of Light* (C. J. Clay and Sons, London, 1904), p. 619.

[2] L. D. Barron, *Molecular Light Scattering and Optical Activity*, 2nd ed. (Cambridge University Press, Cambridge, England, 2004).

[3] G. H. Wagniére, *On Chirality and the Universal Asymmetry: Reflections on Image and Mirror Image* (Wiley-VCH, Weinheim, 2007).

[4] E. Hendry, T. Carpy, J. Johnston, M. Popland, R. V. Mikhaylovskiy, A. J. Lapthorn, S. M. Kelly, L. D. Barron, N. Gadegaard, and M. Kadodwala, Ultrasensitive detection and characterization of biomolecules using superchiral fields, Nat. Nanotechnol. **5**, 783 (2010).

[5] C. Kelly, D. A. MacLaren, K. McKay, A. McFarlane, A. S. Karimullah, N. Gadegaard, L. D. Barron, S. Franke-Arnold, F. Crimin, J. B. Götte, S. M. Barnett, and M. Kadodwala, Controlling the symmetry of inorganic ionic nanofilms with optical chirality, Nat. Commun. **11**, 5169 (2020).

[6] J. Kishine, A. S. Ovchinnikov, and A. A. Tereshchenko, Chirality-Induced Phonon Dispersion in a Noncentrosymmetric Micropolar Crystal, Phys. Rev. Lett. **125**, 245302 (2020).

[7] Y. Togawa, T. Koyama, K. Takayanagi, S. Mori, Y. Kousaka, J. Akimitsu, S. Nishihara, K. Inoue, A. S. Ovchinnikov, and J. Kishine, Chiral Magnetic Soliton Lattice on a Chiral Helimagnet, Phys. Rev. Lett. **108**, 107202 (2012).

[8] Y. Togawa, Y. Kousaka, K. Inoue, and J. Kishine, Symmetry, structure, and dynamics of monoaxial chiral magnets, J. Phys. Soc. Jpn. **85**, 112001 (2016).

[9] B. Göhler, V. Hamelbeck, T. Z. Markus, M. Kettner, G. F. Hanne, Z. Vager, R. Naaman, and H. Zacharias, Spin selectivity in electron transmission through self-assembled monolayers of double-stranded DNA, Science **331**, 894 (2011).

[10] Z. Xie, T. Z. Markus, S. R. Cohen, Z. Vager, R. Gutierrez, and R. Naaman, Spin specific electron conduction through DNA oligomers, Nano Lett. **11**, 4652 (2011).

[11] M. Suda, Y. Thathong, V. Promarak, H. Kojima, M. Nakamura, T. Shiraogawa, M. Ehara, and H. M. Yamamoto, Light-driven molecular switch for reconfigurable spin filters, Nat. Commun. **10**, 2455 (2019).

[12] D. H. Waldeck, R. Naaman, and Y. Paltiel, The spin selectivity effect in chiral materials, APL Mater. **9**, 040902 (2021).

[13] A. Inui, R. Aoki, Y. Nishiue, K. Shiota, Y. Kousaka, H. Shishido, D. Hirobe, M. Suda, J. Ohe, J. Kishine, H. M. Yamamoto, and Y. Togawa, Chirality-Induced Spin-Polarized State of a Chiral Crystal $CrNb_3S_6$, Phys. Rev. Lett. **124**, 166602 (2020).

[14] Y. Nabei, D. Hirobe, Y. Shimamoto, K. Shiota, A. Inui, Y. Kousaka, Y. Togawa, and H. M. Yamamoto, Current-induced bulk magnetization of a chiral crystal $CrNb_3S_6$, Appl. Phys. Lett. **117**, 052408 (2020).

[15] Y. Onuki, A. Nakamura, T. Uejo, A. Teruya, M. Hedo, T. Nakama, F. Honda, and H. Harima, Chiral-structure-driven split Fermi surface properties in $TaSi_2$, $NbSi_2$, and VSi_2, J. Phys. Soc. Jpn. **83**, 061018 (2014).

[16] U. Gottlieb, A. Sulpice, R. Madar, and O. Laborde, Magnetic susceptibilities of VSi_2, $NbSi_2$ and $TaSi_2$ single crystals, J. Phys. Condens. Matter **5**, 8755 (1993).

[17] G. L. J. A. Rikken, J. Fölling, and P. Wyder, Electrical Magnetochiral Anisotropy, Phys. Rev. Lett. **87**, 236602 (2001).

[18] R. Aoki, Y. Kousaka, and Y. Togawa, Anomalous Nonreciprocal Electrical Transport on Chiral Magnetic Order, Phys. Rev. Lett. **122**, 057206 (2019).

[19] G. L. J. A. Rikken and N. Avarvari, Strong electrical magnetochiral anisotropy in tellurium, Phys. Rev. B **99**, 245153 (2019).

[20] The mean free path was calculated by using the electrical conductivity, Fermi wave number, and effective mass for $NbSi_2$ and $TaSi_2$ crystals available in Ref. [15].